Optics Letters

Octave-spanning soliton microcomb in silica microdisk resonators

Jiaxin Gu,[1,†] Xuan Li,[1,†] Kai Qi,[1] Keren Pu,[1] Zhixuan Li,[1] Fan Zhang,[1] Tao Li,[1] ⬤ Zhenda Xie,[1] Min Xiao,[1,2] ⬤ and Xiaoshun Jiang[1,*]

[1]National Laboratory of Solid State Microstructures, College of Engineering and Applied Science and School of Physics, Nanjing University, Nanjing 210093, China
[2]Department of Physics, University of Arkansas, Fayetteville, Arkansas 72701, USA
*Corresponding author: jxs@nju.edu.cn
†These authors contributed equally to this Letter.

We demonstrate a chip-based octave-spanning soliton microcomb in a whispering gallery mode microresonator platform. By fabricating a silica microdisk resonator and optimizing its dispersion with dry etching, we achieve an octave-spanning single-soliton microcomb with a repetition rate of ∼670 GHz at an optical pump power of 162.6 mW. Also, two dispersive waves at the end of the spectrum are observed to extend the comb spectral range and improve the comb power.   © 2023 Optica Publishing Group

Integrated optical frequency combs based on microresonators are promising for many applications [1–3]. Among them, Kerr soliton microcombs with octave-spanning bandwidth for self-referencing are desirable for optical atomic clocks [4] and optical frequency synthesizers [5]. By precisely engineering the dispersion, octave-spanning soliton microcombs have been demonstrated in microring structures with several material platforms, such as silicon nitride [6–9], aluminum nitride [10,11], and lithium niobite [12]. Moreover, dual dispersive waves (DWs) [13] are beneficial to further extend the comb bandwidth and increase the comb power at the ends of the spectrum [7,10]. To achieve such precise dispersion engineering, the variation of the fabricated resonator in dimension should be controlled to within 10 nm [7], which is a huge challenge for fabrication.

Compared with microring structures, chip-based optical microresonators with whispering gallery mode (WGM) structures [14] such as microspheres, microtoroids, as well as microdisks usually exhibit higher optical quality (Q) factors. However, due to the limited dispersion engineering capability, especially the engineering of the locations of the DWs, octave-spanning microcombs in WGM microresonators have only been demonstrated in the modulation instability (MI) state [15,16].

In this work, we demonstrate an octave-spanning soliton microcomb in a WGM microdisk resonator based on a chip-based silica platform that usually exhibits high optical Q factor and low material dispersion. The dispersion of the silica microdisk resonators are optimized by controlling their wedge angles and thicknesses. Also, the locations of the DWs can

be engineered by changing the resonator diameter variation within the micrometer level. The obtained intrinsic Q factor of the dispersion-engineered silica microdisk resonators reaches 1.5×10^7 at the 1550 nm band, which is much larger than that of other platforms [6–12] used for octave-spanning soliton microcomb generation.

The silica microdisk resonator is fabricated by the same dry etching process as in our previous work [17–19]. A typical scanning electron microscopy (SEM) image of it is shown in Fig. 1(a). There are three parameters characterizing the geometric dimensions of the silica microdisk: thickness (T), diameter (D), and wedge angle (α), as illustrated in Fig. 1(b). It is noticed that the wedge angle can be precisely controlled by changing the dry-etching recipe. For example, as shown in Fig. 1(c), the wedge angles of the silica microdisks can be easily controlled by just changing the inductively coupled plasma (ICP) power during the dry-etching process. Two typical SEM images of wedge angles of 25.0° and 32.9° are shown in the insets of Fig. 1(c). Also, the thickness of the silica microdisk can be precisely controlled by the thermal oxidation time during preparation of the thermally grown oxide films [20].

To find the ideal geometry parameters, we use finite element method (FEM) simulations to calculate the resonator dispersion. The variation of the dispersion curve is optimized by comparing with the integrated dispersion D_{int}, defined as the discrepancy between the cavity resonances and the fixed free spectrum range (FSR) around the pump [13]. Here, $D_{int}(\mu) = \omega - \omega_{pump} - D_1\mu = \frac{D_2\mu^2}{2!} + \frac{D_3\mu^3}{3!} + \ldots$, with ω and ω_{pump} being, respectively, the angular frequencies of the cavity resonance and the pump, μ the relative mode number of the resonance with respect to the pump mode, and $D_1/2\pi$ the repetition rate around the pump mode. The generation of the microcomb often requires anomalous dispersion ($D_2 > 0$) with small positive values, so as to afford a larger optical bandwidth for the given pump power and detuning [7].

Here, we focus on the dispersion of the TE fundamental mode family. As it is well known, the cavity dispersion is composed of contributions from both geometrical and material dispersion. We first consider the material dispersion determined only by the material refractive index. We measure the refractive index using an ellipsometer. The measured refractive index is slightly
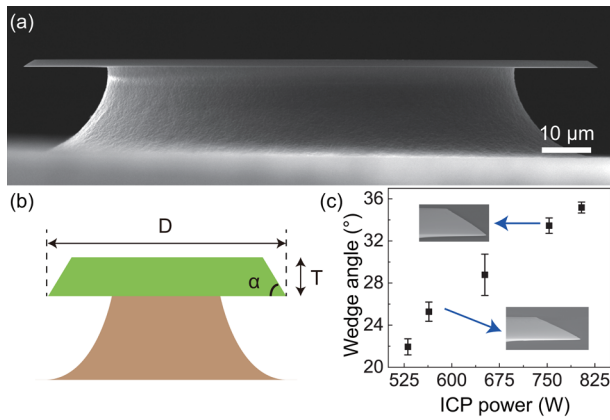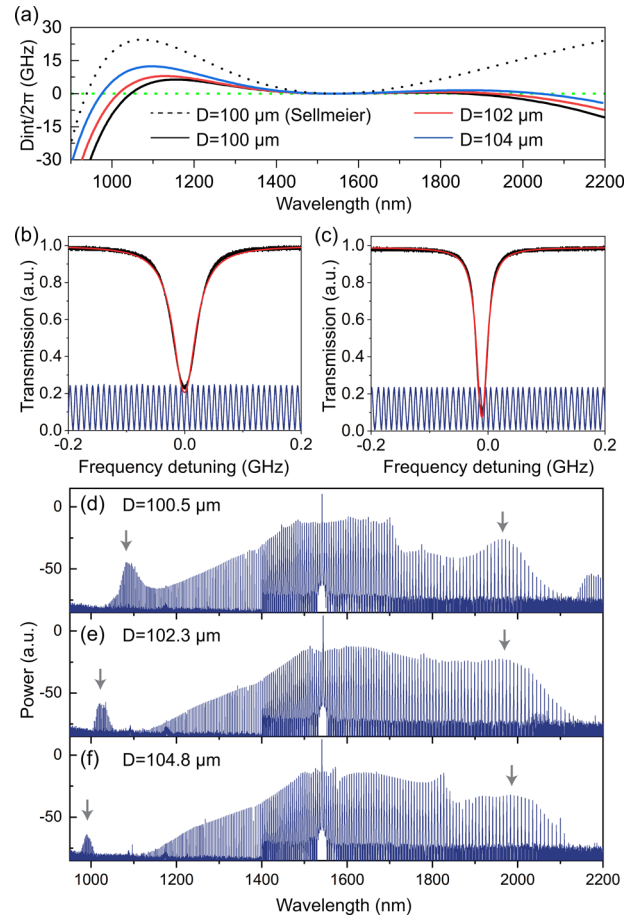
Fig. 1. (a) Typical SEM image of the microdisk (diameter: 100 µm; thickness: 1.3 µm; wedge angle: 32.3°) resonator. (b) Schematic illustration of the geometrical parameters of the silica microdisk: thickness (T), diameter (D), and wedge angle (α). (c) Measured wedge angles using different ICP powers. Insets show two typical SEM images of different wedge angles.

Fig. 2. (a) Simulated integrated dispersion $D_{int}/2\pi$ of the microdisk resonators with a thickness of 1.43 µm and a wedge angle of 32.3° using the measured refractive index (solid line) and the standard Sellemier-equation-defined refractive index (dashed line). Measured transmission spectra of the TE fundamental mode at (b) 1550 nm and (c) 1064 nm bands. The sinusoidal curve is a calibration scan using a fiber Mach–Zehnder interferometer. Broadband optical frequency comb generated in three different samples with diameters of (d) 100.5, (e) 102.3, and (f) 104.8 µm. The gray arrows indicate the positions of the DWs.

different from that of the fused silica defined by the standard Sellmeier equation [21]. We find that such a refractive index variation will reduce D_2 and shift the locations of the DWs closer to the pump [black solid and dashed lines in Fig. 2(a)]. For this reason, we must take the refractive index variation into consideration before discussing the geometrical dispersion.

For practical applications, dual DWs are usually used to generate the broadband microcombs using microring resonators in previous work [7,10]. However, the situation becomes different when involving a microdisk structure, as the optical mode at longer wavelength is confined weaker than at short wavelength due to the absence of the inner sidewall. To increase the confinement of the optical mode at the longer wavelength, we can engineer the microdisk's thickness. We note that the thickness has an impact on dispersion at both short and long wavelengths. As such, when reducing the thickness, the dispersion at short wavelength should be enlarged and one should decrease the wedge angle to compensate for the anomalous dispersion, and vice versa. In brief, we need to choose a suitable thickness and wedge angle to achieve the desired dispersion and dual DWs.

Figure 2(a) shows the optimized $D_{int}/2\pi$ curves of the fundamental TE mode with dual DWs. The thickness of the microdisk is 1.43 µm, the wedge angle is 32.3°, and the diameter varies from 100 µm to 104 µm. As can be seen from the figure, the value of D_2 increases with the location of the DW moving far from the pump when the diameter is increased.

Since measuring the dispersion within a broadband range of hundreds of nanometers is a challenge, here we can evaluate the dispersion of the fabricated microresonators by the generated optical spectra of the microcombs. To measure the broadband microcomb, we first optimize the coupling condition by optimizing the diameter of the fiber taper at the coupling region as well as the coupling distance between the fiber taper and the microresonator using a three-axis piezoelectric stage [22]. Figures 2(b) and 2(c) show the optimized transmission spectra of the TE fundamental modes at 1550 nm and 1064 nm bands, indicating intrinsic Q factors of 1.5×10^7 and 3.5×10^7, respectively. Here, both modes are over-coupled to increase the obtained comb power. As shown in Figs. 2(d)–2(f), we obtain broadband optical microcombs with the fabricated microdisk resonators with diameters of 100.5 µm, 102.3 µm, and 104.8 µm,

respectively. The DW positions are indicated by the gray arrows, which match the same trends as the simulations. Interestingly, we found that the DW locations are less sensitive to the diameter variation within the micrometer scale level, which may make it easier for wafer-scale fabrication using photolithography.

To access the soliton state of the broadband microcomb, we employ the auxiliary-laser-heating method [23–25] to compensate the thermo-optic nonlinearity in the microresonator. As shown in Fig. 3 (a), we use two external cavity diode lasers (ECDLs) as auxiliary laser and pump laser, respectively. In the experiment, both pump and auxiliary lasers are firstly amplified by an erbium-doped fiber amplifier (EDFA), and then pass through the fiber polarization controllers to adjust the polarizations. After that, the pump and auxiliary lasers are coupled into the microdisk resonator through the tapered fiber [22] from the opposite directions. To measure the radio-frequency (RF) noise of the generated microcombs, we use a fiber Bragg grating (FBG), and wavelength division multiplexing (WDM) to filter out the transmitted pump power, as well as the reflected Kerr microcomb generated by the auxiliary laser. The spectra of the
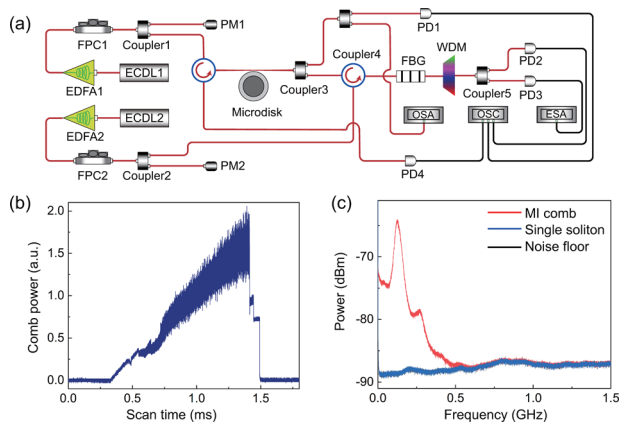
Fig. 3. (a) Schematic of experimental setup for soliton micro-comb generation. FPC, fiber polarization controller; TBF, tunable bandpass filter; PM, power meter; PD, photodiode; OSC, oscillo-scope; ESA, electrical spectrum analyzer. (b) Transmission of comb power with steps indicating the existence of the soliton state. (c) RF noise of the MI comb, single-soliton comb, and noise floor of the PD.
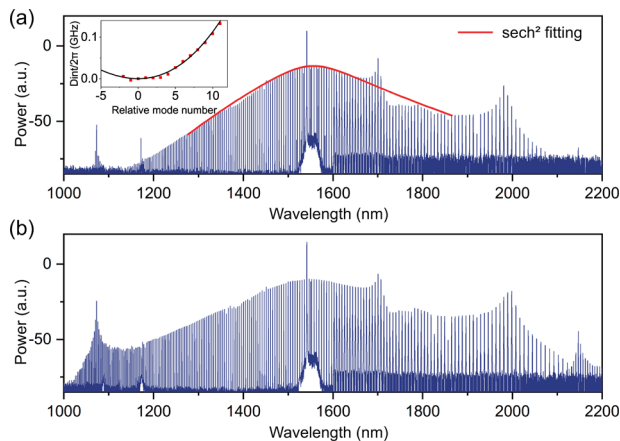
Fig. 4. (a) Near octave-spanning single-soliton microcomb spec-trum with a pump power of 54.1 mW. Inset: measured (dots) and simulated (solid line) dispersions at the 1550 nm band. (b) Octave-spanning single-soliton microcomb spectrum with a pump power of 162.6 mW. The red curve is a sech^2 fitting of the single-soliton spectra.

generated microcombs are measured using two optical spectrum analyzers (OSAs; Yokogawa AQ 6370D and AQ 6375).

In the experiment, we choose the 100.5 μm diameter sil-ica microdisk resonator for octave-spanning soliton microcomb generation. As shown in Fig. 2(b), the loaded Q factor is 4.1×10^6 for the pump mode at a wavelength of 1540.4 nm. Also, we choose a fundamental TM mode at a wavelength of 1548.4 nm as an auxiliary mode whose loaded Q factor is 1.6×10^6. As shown in Fig. 3(b), soliton steps can be clearly obtained in the transmission spectrum. By gradually tuning the pump laser into the soliton steps, we successfully achieve a near-octave single-soliton microcomb (1071.6–2072.7 nm) with a sech^2-shaped spectral envelope at a low pump power (54.1 mW), as shown in Fig. 4(a). During the measurement, the auxiliary laser is thermally locked to the cavity mode with 185.4 mW optical power. Here, the relatively large power of the employed

auxiliary laser is owing to the large thermal optic effect in the silica microdisk resonator and the lower optical Q factor of the auxiliary mode. To further confirm the soliton state, we measure the low RF noise which verifies the high degree of coherence of the comb state from the drastic reduction of the low-frequency intensity noise compared with the MI state [Fig. 3(c)]. By increasing the pump power to 162.6 mW, we successfully obtain an octave-spanning (1023.9–2122.3 nm) single-soliton microcomb [Fig. 4(b)] with a repetition rate of ∼670 GHz. Also, two DWs at the end of the spectrum are obtained to extend the comb spectrum. The relatively lower optical power of the short-wavelength DW is attributed to the larger dispersion. In addition, spatial-mode-interaction-induced DWs [26] are observed at a wavelength of around 1700 nm. During the experiment, we measured the dispersion [as shown in the inset of Fig. 4(a)] of the microdisk resonator at the 1550 nm band, which agrees very well with the simulated results.

In conclusion, we have demonstrated an octave-spanning single-soliton microcomb with two DWs at the end of the spectrum using a dry-etched high-Q-factor silica microdisk resonator. In the future, by further improving the Q factor, opti-mizing the dispersion and the coupling between the fiber taper and the microresonators, we can further lower the operation pump power of the octave soliton microcomb. On the other hand, due to the high Q factor and multi-mode characteristics of the WGM microresonators, recently demonstrated Brillouin–Kerr soliton microcomb [27–29] or injecting a single pump to two close resonances (dual-mode) [30] can be applied to generate the octave-spanning soliton microcomb with easy operation. More-over, an octave-spanning soliton microcomb in the visible band might become possible due to the low material dispersion of silica.

REFERENCES

1. L. Chang, S. Liu, and J. E. Bowers, Nat. Photonics **16**, 95 (2022).
2. T. J. Kippenberg, A. L. Gaeta, M. Lipson, and M. L. Gorodetsky, Science **361**, eaan8083 (2018).
3. W. Wang, L. Wang, and W. Zhang, Adv. Photonics **2**, 1 (2020).
4. Z. L. Newman, V. Maurice, and T. Drake, *et al.*, Optica **6**, 680 (2019).
5. D. T. Spencer, T. Drake, and T. C. Briles, *et al.*, Nature **557**, 81 (2018).
6. Q. Li, T. C. Briles, D. A. Westly, T. E. Drake, J. R. Stone, B. R. Ilic, S. A. Diddams, S. B. Papp, and K. Srinivasan, Optica **4**, 193 (2017).
7. M. H. Pfeiffer, C. Herkommer, J. Liu, H. Guo, M. Karpov, E. Lucas, M. Zervas, and T. J. Kippenberg, Optica **4**, 684 (2017).
8. T. C. Briles, S.-P. Yu, T. E. Drake, J. R. Stone, and S. B. Papp, Phys. Rev. Appl. **14**, 014006 (2020).
9. G. Moille, D. Westly, N. G. Orji, and K. Srinivasan, Appl. Phys. Lett. **119**, 121103 (2021).
10. X. Liu, Z. Gong, A. W. Bruch, J. B. Surya, J. Lu, and H. X. Tang, Nat. Commun. **12**, 5428 (2021).

11. H. Weng, J. Liu, A. A. Afridi, J. Li, J. Dai, X. Ma, Y. Zhang, Q. Lu, J. F. Donegan, and W. Guo, Photonics Res. **9**, 1351 (2021).
12. Y. He, R. Lopez-Rios, Q. Yang, J. Ling, M. Li, K. Vahala, and Q. Lin, in *Conference on Lasers and Electro-Optics, OSA Technical Digest* (Optica Publishing Group, 2021), STu2G.1.
13. V. Brasch, M. Geiselmann, T. Herr, G. Lihachev, M. H. Pfeiffer, M. L. Gorodetsky, and T. J. Kippenberg, Science **351**, 357 (2016).
14. K. J. Vahala, Nature **424**, 839 (2003).
15. P. Del'Haye, T. Herr, E. Gavartin, M. Gorodetsky, R. Holzwarth, and T. J. Kippenberg, Phys. Rev. Lett. **107**, 063901 (2011).
16. H. Chen, Q. Ji, H. Wang, Q. Yang, Q. Cao, Q. Gong, X. Yi, and Y. Xiao, Nat. Commun. **11**, 2336 (2020).
17. G. Li, P. Liu, X. Jiang, C. Yang, J. Ma, H. Wu, and M. Xiao, Photonics Res. **3**, 279 (2015).
18. J. Ma, L. Xiao, J. Gu, H. Li, X. Cheng, G. He, X. Jiang, and M. Xiao, Photonics Res. **7**, 573 (2019).
19. J. Gu, J. Liu, Z. Bai, H. Wang, X. Cheng, G. Li, M. Zhang, X. Li, Q. Shi, M. Xiao, and X. Jiang, Photonics Res. **9**, 722 (2021).
20. D. Y. Oh, S. A. Diddams, S. B. Papp, and K. J. Vahala, Nat. Photonics **10**, 316 (2016).
21. M. J. Weber, *Handbook of Optical Materials* (CRC Press, 2002).
22. M. Cai, O. Painter, and K. J. Vahala, Phys. Rev. Lett. **85**, 74 (2000).
23. H. Zhou, Y. Geng, W. Cui, S.-W. Huang, Q. Zhou, K. Qiu, and C. Wei Wong, Light: Sci. Appl. **8**, 50 (2019).
24. S. Zhang, J. M. Silver, L. Del Bino, F. Copie, M. T. M. Woodley, G. N. Ghalanos, A. Ø. Svela, N. Moroney, and P. Del'Haye, Optica **6**, 206 (2019).
25. Y. Zhao, L. Chen, C. Zhang, W. Wang, H. Hu, R. Wang, X. Wang, S. T. Chu, B. Little, W. Zhang, and X. Zhang, Laser Photonics Rev. **15**, 2100264 (2021).
26. Q. Yang, X. Yi, K. Y. Yang, and K. Vahala, Optica **3**, 1132 (2016).
27. Y. Bai, M. Zhang, Q. Shi, S. Ding, Y. Qin, Z. Xie, X. Jiang, and M. Xiao, Phys. Rev. Lett. **126**, 063901 (2021).
28. K. Jia, X. Wang, D. Kwon, J. Wang, E. Tsao, H. Liu, X. Ni, J. Guo, M. Yang, X. Jiang, J. Kim, S.-n. Zhu, Z. Xie, and S.-W. Huang, Phys. Rev. Lett. **125**, 143902 (2020).
29. I. H. Do, D. Kim, D. Jeong, D. Suk, D. Kwon, J. Kim, J. H. Lee, and H. Lee, Opt. Lett. **46**, 1772 (2021).
30. H. Weng, A. A. Afridi, J. Li, M. McDermott, H. Tu, L. P. Barry, Q. Lu, W. Guo, and J. F. Donegan, APL Photonics **7**, 066103 (2022).